Hindawi
Advances in Civil Engineering
Volume 2024, Article ID 8888139, 12 pages
https://doi.org/10.1155/2024/8888139

Research Article

Assessment of Reinforcement Effect of FRP-Strengthened Shield Segment Joint Based on the CZM Model

Jianjun Kuang,[1] Yuanqing Chen,[2] Xiaofei Li,[3] Wei Guo,[4] Jia Li,[5] and Yiqun Huang[6]

[1]*China Communications Construction Co., Ltd., Beijing, China*
[2]*Xiamen Metro Construction Co., Ltd., Xiamen, China*
[3]*CCCC First Highway Engineering Xiamen Co., Ltd., Xiamen, China*
[4]*Shanghai Jianke Engineering Consulting Co., Ltd, Shanghai, China*
[5]*Jianfa Hecheng Engineering Consulting Co., Ltd., Xiamen, China*
[6]*Fujian University of Technology, Fuzhou, China*

Correspondence should be addressed to Yiqun Huang; yiqunhuang@fjut.edu.cn

Received 6 December 2023; Revised 18 February 2024; Accepted 25 April 2024; Published 9 May 2024

Academic Editor: Tingting Zhang

Copyright © 2024 Jianjun Kuang et al. This is an open access article distributed under the Creative Commons Attribution License, which permits unrestricted use, distribution, and reproduction in any medium, provided the original work is properly cited.

As the weakest link in the shield segment, the reinforcement and repair technology of shield segment joint has received widespread attention. In this study, an finite element model utilizing a cohesive zone model (CZM) was constructed to simulate the mechanical behavior of the shield segment joint during the whole fracture process. The proposed modeling method of joint allows multiple layers of steel bars to be stacked without interference by applying cohesive elements. Cohesive elements were employed to represent the mechanical response of potential fracture surfaces in concrete, as well as the interfaces between steel–concrete and fiber-reinforced polymer (FRP)–concrete, by utilizing various constitutive models tailored for mixed-mode loading conditions. A group of experiments was chosen to assess the precision of the proposed model by comparing the mechanical response and the fracture patterns. Finally, parameter analyses were conducted to study the reinforcement effect of the FRP bonding length and width on the shield segment joint. The results indicate that external bonding of FRP can effectively enhance the bearing capacity and stiffness of shield segment joints. However, insufficient bonding length or width may significantly reduce the strengthening effect and potentially decrease the ductility of the joint.

1. Introduction

With the development of subway construction, the sealing and safety of shield tunnel segments have attracted widespread attention and research. Tunnels in service are subjected to a combination of factors during operation, including surrounding rock pressure, groundwater pressure, and surface and adjacent structure construction loads. The mechanical performance of tunnel structures deteriorates over time due to the prolonged influence of these combined loads, resulting in stress losses at the joints [1]. When the contact stress state at the pipe segment joints deteriorates to a certain extent, joint leakage can occur.

To investigate the mechanical behavior of the shield segment joint, in order to investigate the mechanical performance of shield tunnel segment joints, researchers have conducted a series of experiments and theoretical studies. For experimental studies, researchers typically utilize a four-point bending setup (or other experimental setup) to conduct load capacity tests on prototype pipe segment joints [2–7]. These approaches were employed to examine the stiffness, strength, and failure modes of the shield segment joints. For theoretical or numerical studies, researchers primarily analyze pipe segment joints using spring-based theoretical models or finite element (FE) models [8–13]. These analytical methods are effective in reflecting the macroscopic mechanical properties of the joints, such as the moment–rotation relationship. However, for detailed fracture behavior, existing models have certain limitations. Besides, researchers have conducted numerous studies on the reinforcement and repair of pipe segment joints. However, these studies predominantly utilize reinforcements, such as steel plates, steel fibers, or steel pipes [14–20]. In environments where there is water present, these steel reinforcements are

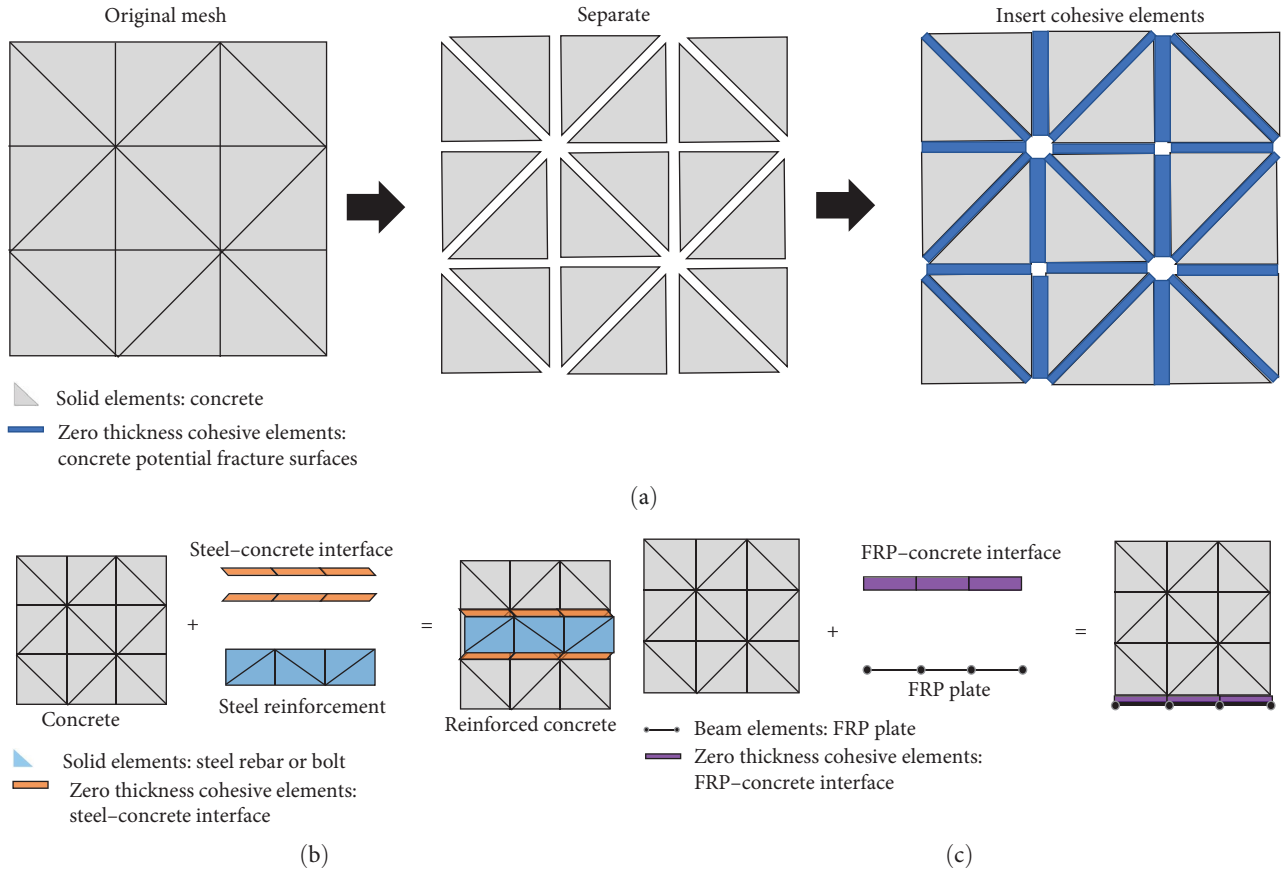

Figure 1: Modeling of the FRP strengthened RC based on the CZM: (a) modeling of concrete; (b) modeling of the reinforcement and steel–concrete interface; and (c) modeling of the FRP and FRP–concrete interface.

susceptible to corrosion, which imposes certain limitations on their practical application. Therefore, there is a promising application potential in reinforcing segment joints using non-corrosive fiber-reinforced polymer (FRP) materials.

To enhance the simulation of the mechanical and fracture characteristics of the FRP-reinforced shield segment joint, an adequately detailed model is required to simultaneously simulate concrete cracking, the slip and debonding between steel reinforcement and concrete, as well as the interface mechanical properties between FRP and concrete. Traditional FE continuum element models are inadequate in accurately representing such problems. Hence, there is a pressing need to develop new models suitable for analyzing systems with a large number of interface issues. Therefore, the cohesive zone modeling (CZM) approach [21–28] is a preferable choice, since its primary advantage lies in its ability to accurately characterize the mechanical behavior of interfaces, such as the interaction between cracks in concrete before and after cracking, as well as the interface mechanical properties between different materials.

In this study, a numerical modeling approach for FRP-reinforced shield segment joints based on CZM is proposed. By using the zero-thickness cohesive elements, this model can simultaneously analyze the interfaces between FRP and concrete, steel reinforcement and concrete, concrete and concrete, and concrete and rubber. Additionally, through secondary development, the constitutive relationships applicable to different interfaces have been implemented in the model. Experimental data have been employed to confirm the precision of the proposed model, considering aspects such as load-bearing capacity, stiffness, ductility, and failure mode. Finally, the strengthening effect of CFRP plate on the shield segment joint is analyzed with different reinforcing parameters.

2. CZM Model of the Shield Segment Joint

2.1. Modeling Method of the Joint. The CZM was applied to simulate the FRP-strengthened shield segment joint. The joint of shield segment is essentially a reinforced concrete structure. Thus, the modeling method proposed previously [24, 27] was adopted to build up the FE model of joint. As shown in Figure 1, the procedure for constructing the FE model is outlined as follows:

Step 1: Separate the concrete original mesh (solid elements), and insert concrete potential fracture surfaces (cohesive elements with zero thickness) to build up the CZM of concrete.

Step 2: Insert the steel reinforcement (solid elements) and steel–concrete interface (zero-thickness cohesive elements) to establish the RC model.

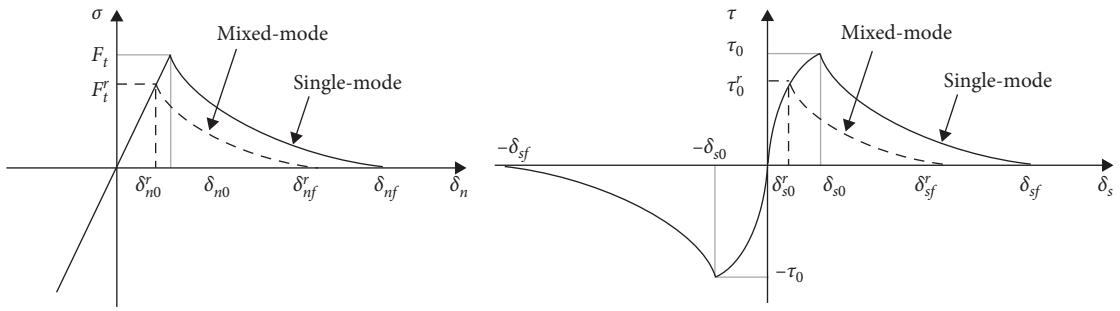

Figure 2: Single-mode stress–displacement relation: (a) normal direction and (b) tangential direction.

Step 3: Insert the FRP plate (beam elements) and FRP–concrete interface (zero-thickness cohesive elements) to model the FRP-strengthened RC.

It should be noticed that in step 2, the steel was inserted to the model by the connection of cohesive elements. Therefore, multilayer of steel reinforcement or bolt can be inserted together, and they will not interfere with each other.

2.2. Constitutive Models for FRP–Concrete Interface and Concrete Potential Fracture Surfaces

2.2.1. Damage Relation under Mixed-Mode Condition. The damage constitutive models proposed previously [24, 27] were employed to characterize the mechanical behavior of FRP–concrete interface and concrete potential fracture surfaces. As shown in Figure 2, the stress–displacement behavior for both interfaces under single-mode conditions can be described as follows:

(1) Normal direction:

$$\sigma = \begin{cases} k_n\delta_n, & \delta_n \le \delta_{n0} \\ (1-D)k_n\delta_n, & \delta_{n0} < \delta_n \le \delta_{nf} \\ 0, & \delta_n > \delta_{nf} \end{cases}, \tag{1}$$

where σ is the normal stress, k_n is stiffness in the normal direction, δ_n is the displacement in the normal direction, δ_{n0} and δ_{nf} are the key parameters of damage state, as shown in Figure 2(a), and D is the damage coefficient (or damage factor), and it can be calculated by the following equation:

$$D = \begin{cases} 1 - \dfrac{\delta_{n0}}{\delta_n}\exp\left[\dfrac{10\delta_{\mathrm{n0}}}{\delta_{\mathrm{n0}} - \delta_{\mathrm{nf}}}\left(\dfrac{\delta_{\mathrm{n}}}{\delta_{\mathrm{n0}}} - 1\right)\right] (\delta_{\mathrm{n0}} \le \delta_{\mathrm{n}} \le \delta_{\mathrm{nf}}), \text{FRP} - \text{concrete interace} \\ \dfrac{(\delta_n - \delta_{n0})\delta_f}{(\delta_{nf} - \delta_{n0})\delta_n}\left(\delta_{n0} \le \delta_n \le \delta_{nf}\right), \text{concrete potential fracture surfaces} \end{cases}. \tag{2}$$

(2) Tangential direction:

$$\tau = \begin{cases} k_s\delta_s, & |\delta_s| \le \delta_{s0} \\ (1-D)\dfrac{\tau_0}{\delta_{s0}}\delta_s, & \delta_{s0} < |\delta_s| \le \delta_{sf} \\ 0, & |\delta_s| > \delta_{sf} \end{cases}, \tag{3}$$

where τ is the shear stress; k_s is stiffness in the tangential direction, it is a constant parameter for concrete potential fracture surfaces, for FRP–concrete interface, $k_s = \tau_0/(\delta_{s0}|\delta_s|)^{0.5}$ $(|\delta_s| \le \delta_{s0}|)$; δ_s is the tangential displacement; δ_{s0} and δ_{sf} are the key parameters of damage state, as shown in Figure 2(b).

In the tangential direction, the damage coefficient can be calculated by the following equation:

$$D = \begin{cases} 1 - \dfrac{\delta_{s0}}{|\delta_s|}\exp\left[\dfrac{10\delta_{\mathrm{s0}}}{\delta_{\mathrm{s0}} - \delta_{\mathrm{sf}}}\left(\dfrac{|\delta_{\mathrm{s}}|}{\delta_{\mathrm{s0}}} - 1\right)\right] (\delta_{\mathrm{s0}} \le |\delta_{\mathrm{s}}| \le \delta_{\mathrm{sf}}), \text{FRP} - \text{concrete interace} \\ \dfrac{(|\delta_s| - \delta_{s0})\delta_f}{(\delta_{sf} - \delta_{s0})|\delta_s|}\left(\delta_{s0} \le |\delta_s| \le \delta_{sf}\right), \text{concrete potential fracture surfaces} \end{cases}. \tag{4}$$

Defining the total displacements [24, 27] as follows:

$$\begin{cases} \delta = \sqrt{\langle \delta_n \rangle^2 + \delta_s^2} \\ \delta_0 = \sqrt{\delta_{n0}^{r^2} + \delta_{s0}^{r^2}} \\ \delta_f = \sqrt{\delta_{nf}^{r^2} + \delta_{sf}^{r^2}} \end{cases}, \tag{5}$$

where δ is the total displacement; δ_0 is the displacement of the damaged initial state in the mixed-mode; δ_f is the displacement of the failure state in the mixed-mode; δ_{n0}^r, δ_{s0}^r, δ_{nf}^r, and δ_{sf}^r are the key parameters of damage state [24, 27], as shown in Figure 2.

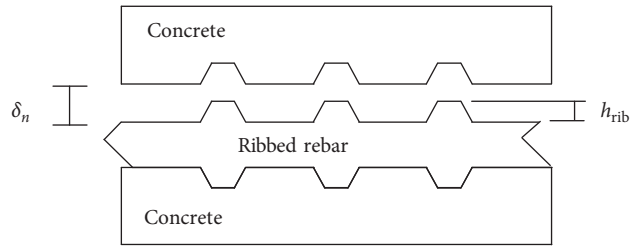

Figure 3: Normal separation of the steel–concrete interface (ribbed rebar).

Based on the total displacements defined above, in the mixed-mode condition, the damage coefficient D can be defined as follows:

$$D = \begin{cases} 1 - \dfrac{\delta_0}{\delta} \exp\left[\dfrac{10\delta_0}{\delta_0 - \delta_{\text{f}}}\left(\dfrac{\delta}{\delta_0} - 1\right)\right], \text{FRP} - \text{concrete interace} \\ \dfrac{(\delta - \delta_0)\delta_f}{(\delta_f - \delta_0)\delta}, \text{concrete potential fracture surfaces} \end{cases} \quad (\delta_0 \le \delta \le \delta_f). \tag{6}$$

2.2.2. Friction Effect. The friction effect [24, 27] was also considered into the calculation of stress. According to the different slip conditions, the friction stress can be calculated as follows:

(1) Interfacial nonsliding condition.

In the interfacial nonsliding condition, the shear stress can be transmitted normally. Thus, the friction stress T_f can be given as follows:

$$T_f = k_s\left(\delta_s - \delta_s^{\text{slide}}\right)\left(\left(\delta_s - \delta_s^{\text{slide}}\right) \le \frac{T_{f\max}}{k_s}\right), \tag{7}$$

where δ_s^{slide} is the interfacial slip which has been generated during the fracture process, and $T_{f\max}$ is the maximum friction stress, and it can be calculated by the following equation:

$$T_{f\max} = f\langle -k_n\delta_n \rangle, \tag{8}$$

where f is the friction coefficient.

(2) Interfacial sliding condition.

In the interfacial sliding condition, the friction stress can be calculated by the following equation:

$$\begin{cases} T_f = f|k_n\delta_n| \dfrac{\delta_s - \delta_s^{\text{slide}}}{\left|\delta_s - \delta_s^{\text{slide}}\right|} \\ \delta_s^{\text{slide}^*} = \delta_s - \dfrac{T_f}{k_s} \end{cases} \left(\left(\delta_s - \delta_s^{\text{slide}}\right) > \frac{T_{f\max}}{k_s}\right), \tag{9}$$

where $\delta_s^{\text{slide}^*}$ is the slip displacement which has been updated.

2.2.3. Expression of Stresses. Finally, incorporating the damage relation and friction effect, the stress can be expressed as follows:

(1) Normal stress:

$$\sigma = \begin{cases} k_n\delta_n, & \delta_n \le \delta_{n0}^r \\ (1 - D)k_n\delta_n, & \delta_{n0}^r < \delta_n \le \delta_{nf}^r \\ 0, & \delta_n > \delta_{nf}^r \end{cases}, \tag{10}$$

(2) Shear stress:

$$\tau = \begin{cases} k_s\delta_s, & \delta \le \delta_0 \\ (1 - D)\dfrac{\tau_0^r}{\delta_{s0}^r}\delta_s + D \cdot T_f, & \delta_0 < \delta \le \delta_f \\ T_f, & \delta > \delta_f \end{cases}. \tag{11}$$

2.3. Constitutive Models of the Steel–Concrete Interface (Ribbed). The mixed-mode constitutive model [24, 27] considering the influence of interfacial normal separation was adopted in this study. According to Figure 3, a weakening factor D_2 can be defined as follows:

$$D_2 = \begin{cases} 1, & \delta_n \le 0 \\ (h_{\text{rib}} - \delta_n)/h_{\text{rib}}, & 0 < \delta_n < h_{\text{rib}} \\ 0, & \delta_n \ge h_{\text{rib}} \end{cases}, \tag{12}$$

Where h_{rib} is the height of the rib of reinforcement, as shown in Figure 3.

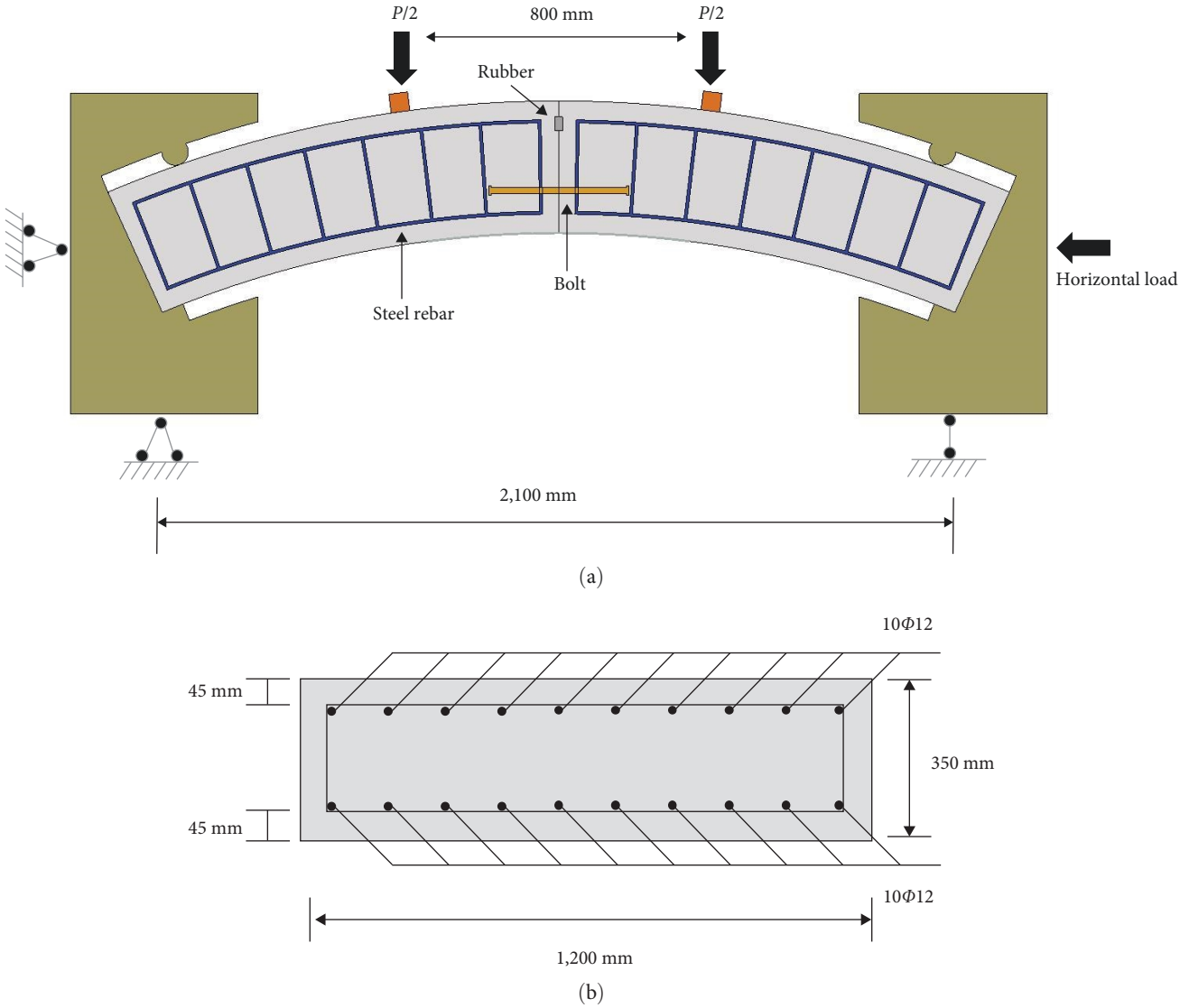

FIGURE 4: Load scheme and geometry of the segment joint: (a) load scheme and (b) geometry information of the segment section.

Based on the weakening factor D_2, the modified bond-slip relation (recommended by CEB-FIP [29]) of the reinforcement–concrete interface can be given as follows:

$$\tau = D_2 \cdot \begin{cases} \tau_{\max}\left(\dfrac{\delta_s}{\delta_{s1}}\right)^{\alpha}, & \delta_s \le \delta_{s1} \\ \tau_{\max} - (\tau_{\max} - \tau_{\text{res}})\left(\dfrac{\delta_s - \delta_{s1}}{\delta_{s2} - \delta_{s1}}\right), & \delta_{s1} < \delta_s < \delta_{s2} \\ \tau_{\text{res}}, & \delta_s \ge \delta_{s2} \end{cases}, \tag{13}$$

where $\tau_{\max}$ is the bond strength, τ_{res} is the residual stress, δ_{s1} and δ_{s2} are the displacements in the tangential direction which corresponding to the bond strength and residual stress, and α is the constant parameter about stiffness. For ribbed rebar, $\tau_{\max} = (f_{ck})^{0.5}$ (f_{ck} is the concrete compression strength), $\tau_{\text{res}} = 0.15 \cdot \tau_{\max}$, $\delta_{s1} = 0.6$ mm, $\delta_{s2} = 2.5$ mm, $\alpha = 0.4$. As for plain rebar, $\tau_{\max} = \tau_{\text{res}} = 0.1 \times (f_{ck})^{0.5}$, $\delta_{s1} = 0.01$ mm, $\alpha = 0.5$.

3. Validation of the Numerical Model

To assess the precision of the FE model proposed in this study, a group of shield segment joint experiments [30] was chosen to be compared with the simulation results. Figure 4 shows the simplified load scheme and geometry of the segment joint. The outer diameter of the segment is 6.2 m, and the inner diameter of the segment is 5.5 m. The center angle of each segment is 22°, and the thickness of the segment is 1.2 m. Concrete with a design strength of 55 MPa and steel ribbed rebar with a yield strength of 400 MPa were used to cast the shield segment. Besides, two 30 mm-diameter bolts with 400 mm longitude and 400 MPa yield strength were used to connect two segments.

As shown in Figure 4, the shield segment is placed in two concave rigid frames, where the left rigid frame is hinged on the left and bottom sides, while the right rigid frame is supported by roller bearings at the bottom and subjected to horizontal thrust on the right side. The upper part of the

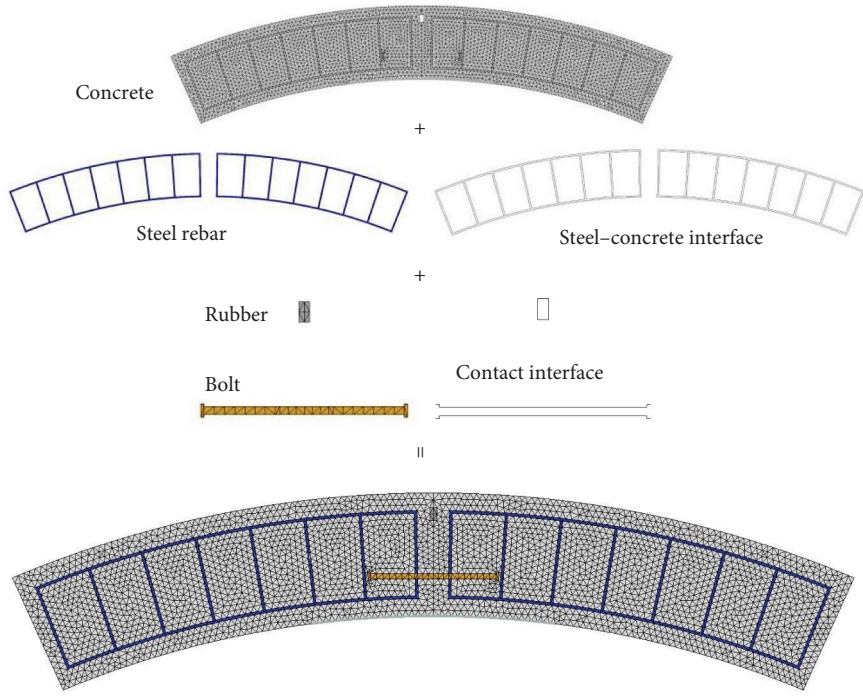

Figure 5: Composition of the segment joint FE model.

Table 1: Material parameters for cohesive elements.

Material	Normal direction			Tangential direction			
	k_n (GPa/m)	F_t (MPa)	G_n (N·m)	k_s (GPa/m)	$\tau_0(\tau_{\max})$ (MPa)	G_s (N·m)	f
Concrete potential fracture surface	10^6	2.80	110	10^6	9.80	1,100	0.35
Rebar–concrete Interface (ribbed)	10^6	0.50	20	—	6.70	—	—
Contact interface	10^6	0	0	10^6	0	0	0.35

specimen is subjected to a pair of vertical loads spaced 800 mm apart, resulting in the joint becoming a pure bending section. During the loading process, the ratio of bending moment to horizontal load is 300 mm.

The structure of the FE model is illustrated in Figure 5. The FE model consists of concrete, steel rebar, steel–concrete interface, rubber, bolt, and contact interface. The constitutive model applied to the contact interface is identical to that used for the potential fracture surfaces of concrete, with a very low normal and shear strength. There are about 20,000 nodes, 6,500 triangular elements (CPS3), and 12,000 cohesive elements (COH2D4) in a typical FE model. In this model, the concrete, steel rebar, bolt, and rubber are represented by solid elements. To ensure that the area of steel–concrete interface is consistent with the actual one, the width of the rebar is set to its radium R. Thus, the out-of-plane thickness of the steel–concrete interface can be set to πR. In addition, there is a 4 mm gap between the segments above the waterstop rubber. In the model, although there is no gap at this contact surface, it is set to have a contact stress after mutual penetration of 4 mm.

All the constitutive adopted in this study were implemented through ABAQUS subroutine VUMAT [31], the model was solved with the ABAQUS/EXPLICITE solver [31] by using a quasistatic method. The principle of this method is to solve static problems using dynamic solution methods. Its advantage lies in avoiding the convergence difficulties encountered in static solution.

According to the experimental results, repeat trials, and the relative references about CZM [21–27], the material parameters utilized in the cohesive elements are detailed in Table 1. Additionally, concrete has an elastic modulus E of 30 GPa and a Poisson's ratio v of 0.2. Steel has an elastic modulus E of 30 GPa, a Poisson's ratio v of 0.2, and a yield strength of 390 MPa. Rubber has an elastic modulus E of 20 MPa and a Poisson's ratio v of 0.4.

Figure 6 shows the result of the simulation. By deleting cohesive elements with a damage factor reaching 1, the cracks

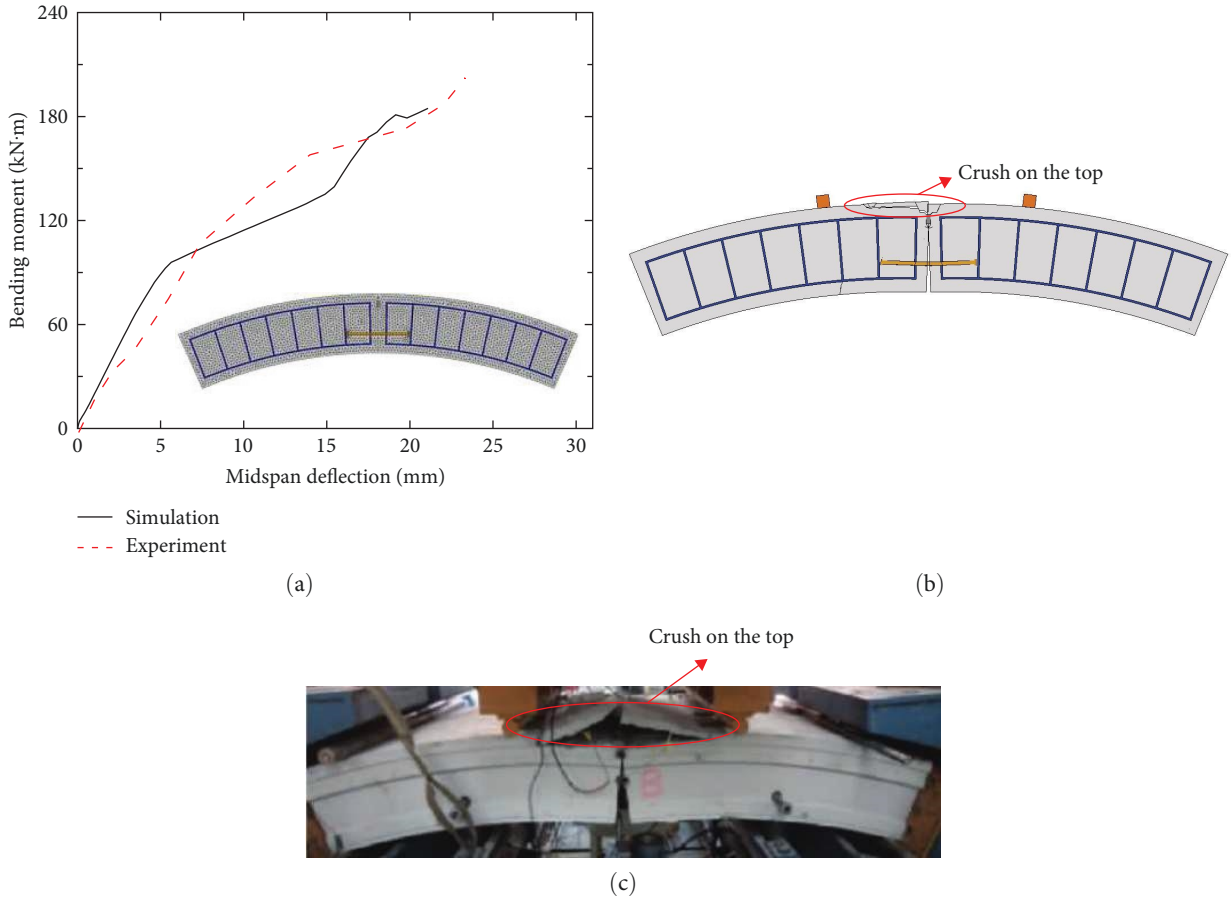

FIGURE 6: Simulation results of the joint numerical model: (a) bending moment–defletion curve; (b) fracture pattern of model; and (c) fracture pattern of the experimental specimen [30].

in the model can be represented. The fracture process is as follows: At first, the bending moment increased linearly with the increment of midspan deflection; subsequently, the bolt entered the yield stage, which leaded that the slope of the bending moment–deflection curve undergoes a reduction. Finally, the concrete above the rubber makes contact, and the stiffness of the joint increases, causing the slope of the curve to recover until the upper concrete crushed, as shown in Figures 6(a) and 6(b). By comparing the bending moment–deflection curve and the fracture pattern between simulation and experiments, the simulation results closely match the experimental data, indicating that the proposed numerical model accurately captures the mechanical behavior of the shield segment joint.

4. Analysis of the FRP-Strengthened Shield Segment Joint

The strengthening effect of the FRP on the shield segment joint is assessed based on the proposed CZM model. Due to the varying dimensions of existing engineering shield segment, in order to facilitate the comparison of the mechanical performance of joints before and after reinforcement, the same joint form and material parameters as those in Section 3 were selected. The composition of the FRP-strengthened shield segment joint is as shown in Figure 7. The FRP plate is connected to the segment joint through FRP–concrete interface (zero-thickness cohesive elements).

According to the relative references [26, 27, 32], the CFRP plate was chosen as the external reinforcement. The CFRP plate is set to bond under the whole bottom of shield segments. The CFRP plate has a width of 1.2 m and a thickness of 1.2 mm. The material parameters of the FRP–concrete interface are listed in Table 2. It should be noted that due to the various types of epoxy resins, the parameters of the FRP–concrete interface also vary. Therefore, the parameters used in this paper mainly refer to those used in previous studies [26, 27, 32]. Besides, the CFRP plate has an elastic modulus E of 165 GPa.

Figure 8 shows enhancement provided by the externally bonded CFRP plate. Through the bending moment–deflection curve, as shown in Figure 8(a), the stiffness and the bearing capacity of the joint is significantly strengthened, the maximum bending moment and the stiffness are approximately 2.5 times and 1.7 times that of the original join. Besides, the fracture pattern of the joint is changed. Since the bottoms of the segments are connected by the CFRP plate (CFRP plate plays a role similar to steel rebar, as shown in Figures 8(c) and 8(d)), the joint is transformed into an integral RC structure. Thus, when the joint fails, several cracks will initiate at the bottom of

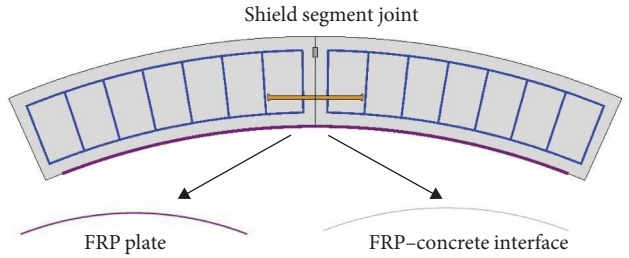

Figure 7: Composition of the FRP-strengthened shield segment jont.

Table 2: Material parameters of the FRP–concrete interface.

Material	Mode I			Mode II			
	k_n (GPa/m)	F_t (MPa)	G_n (N·m)	k_s (GPa/m)	$\tau_0(\tau_{max})$ (MPa)	G_s (N·m)	f
FRP–concrete interface	200	1.10	60	—	3.30	300	0.35

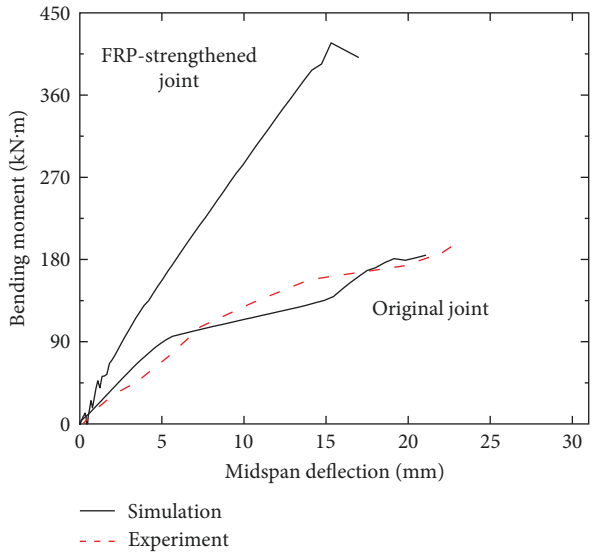

(a)

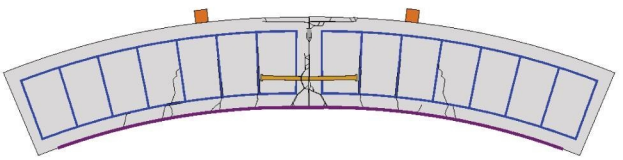

(b)

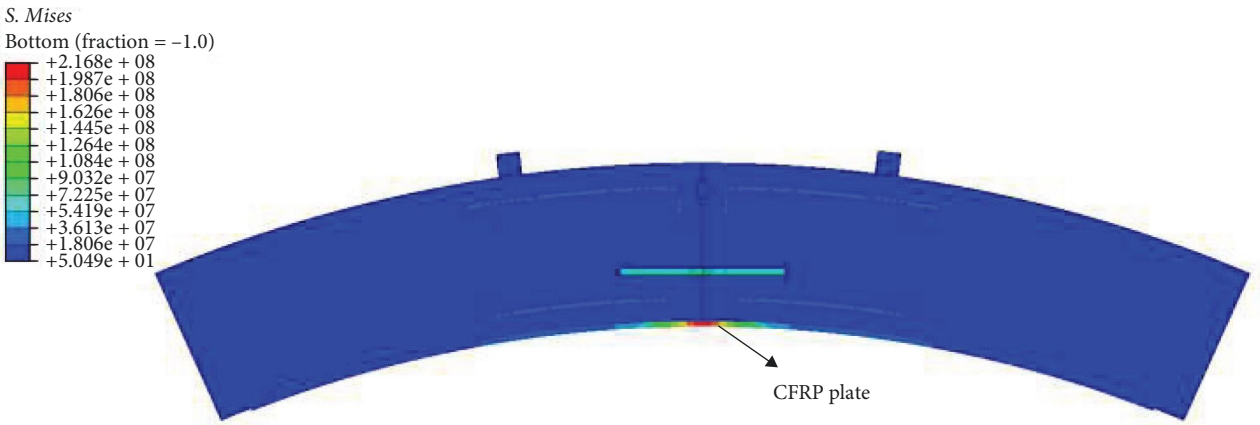

(c)

Figure 8: Continued.

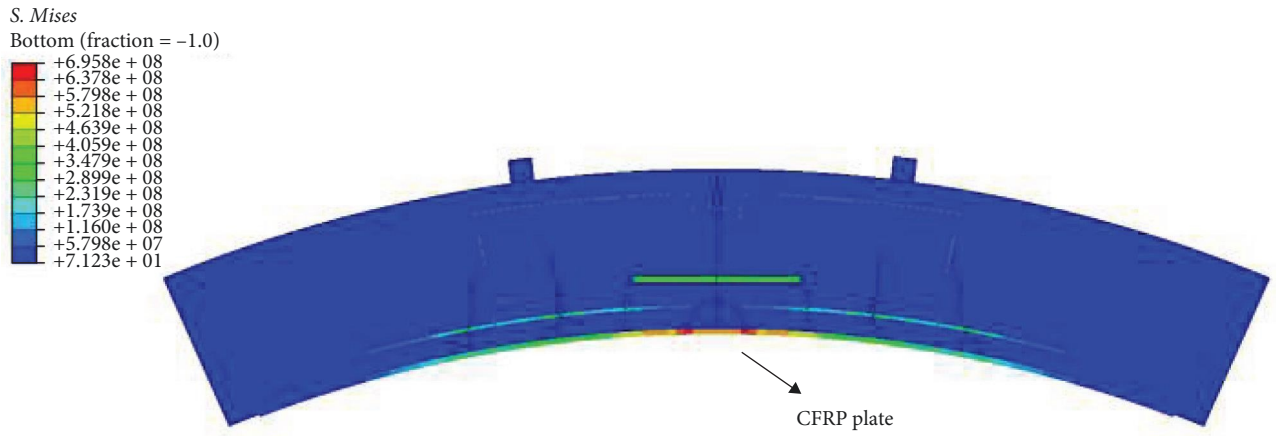

(d)

Figure 8: Simulation results of the FRP-strengthened segment joint: (a) bending moment–deflection curve; (b) fracture pattern; (c) stress distribution in the elastic stage; and (d) stress distribution when crack occured.

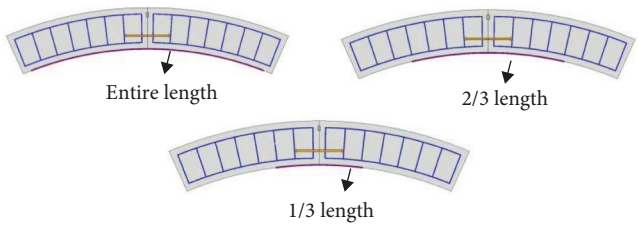

Figure 9: Three types of segment joints with different bonding length.

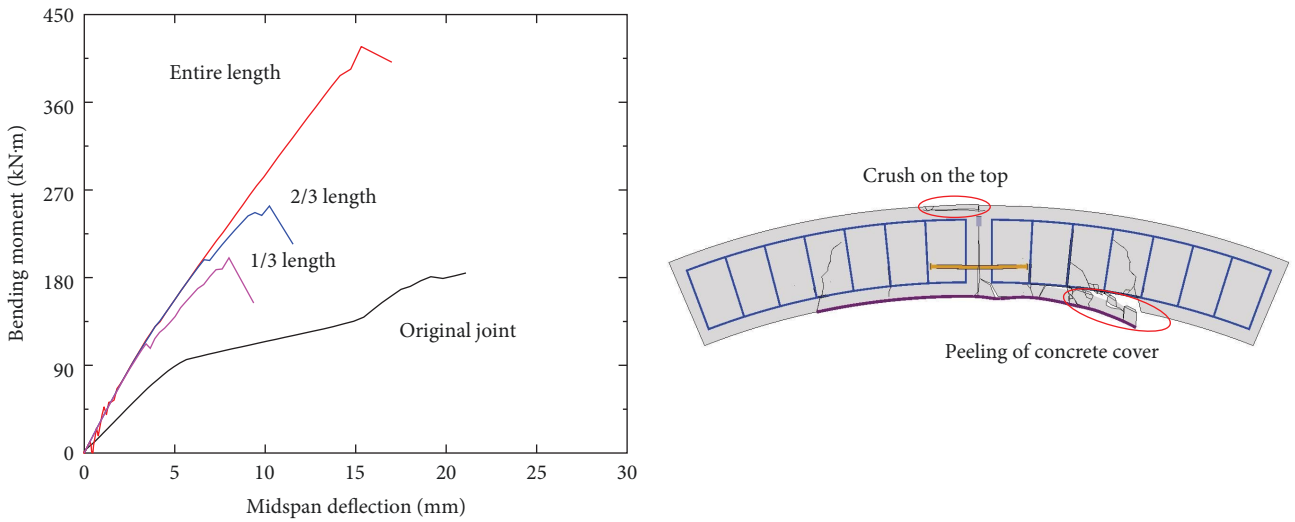

(a) (b)

Figure 10: Simulation results with different bonding length: (a) bending moment–deflection curves and (b) typical fracture pattern of the joint with insufficient bonding length.

segment concrete and propagate upward, with the crush of the top concrete. This fracture pattern is very similar to the traditional RC beam. However, it should be noticed the application of CFRP plate will reduce the ductility of the joint.

4.1. Influence of the Bonding Length. In this section, the effect of the CFRP bonding length on the segment joint is investigated. As shown in Figure 9, three types of segment joints with different bonding length (entire length, 2/3 length, and

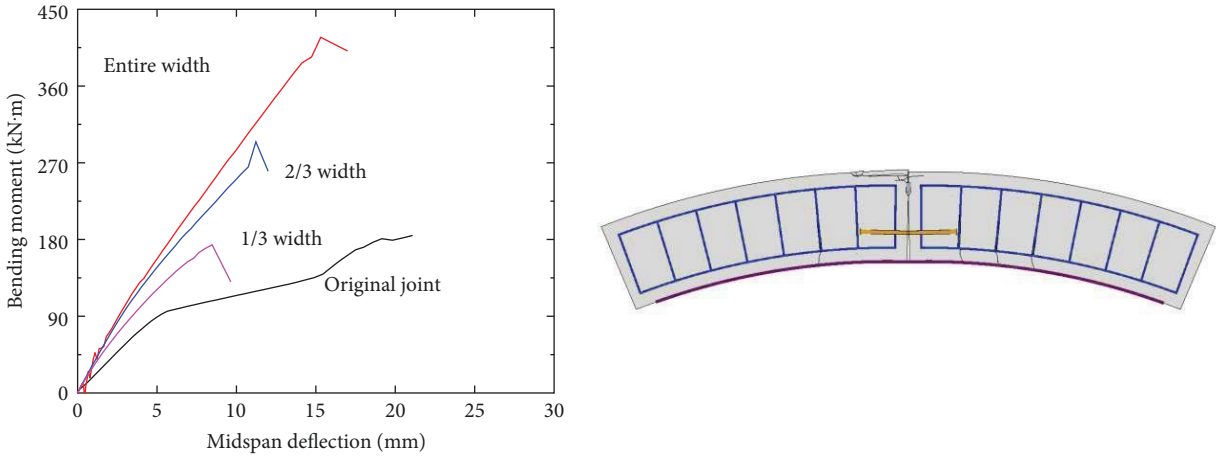

FIGURE 11: Simulation results with different bonding width: (a) bending moment-deflection curves; and (b) typical fracture pattern of the joint with insufficient bonding width.

1/3 length) were simulated. All the material parameters are the same to Sections 3 and 4.

Figure 10 shows the simulation results of the FRP-strengthened segment joint with different bonding lengths. The joint with the entire bonding length has the best strengthening effect. However, with the 2/3 and 1/3 bonding length, both the bearing capacity and ductility of the joint are substantially decreased, as shown in Figure 10(a). Besides, with the insufficient bonding length, the fracture pattern will also be changed. As shown in Figure 10(b), when the joint fails, the concrete cover will peel off, and this ultimately leads to the failure of the CFRP strengthening effect.

4.2. Influence of the Bonding Width. In this section, the effect of the CFRP bonding width on the segment joint is investigated. The CFRP-strengthened joint with different bonding width (1.2, 0.8, and 0.4 m corresponding to entire width, 2/3 width, 1/3 width) were simulated. Figure 11 shows the influence of the bonding width of CFRP plate. Reduced bonding width leads to a significant decrease in joint stiffness, bearing capacity, and ductility. Furthermore, as depicted in Figure 11(b), the fracture pattern with insufficient CFRP width appears similar to the one without an externally bonded CFRP plate. These results indicates that when the CFRP plate's cross-sectional stiffness is insufficient, its reinforcement effectiveness is significantly compromised.

5. Conclusions

This study introduces a FE model for simulating the FRP-strengthened shield segment joint using the CZM. Cohesive elements were utilized to characterize the concrete potential fracture surfaces, as well as the interfaces between FRP and concrete, and between steel and concrete. The corresponding constitutive models were adopted to characterize these components. A group of experiments of segment joint was chosen to evaluate the simulation accuracy. The simulation results fit well with the experimental one.

Based on the proposed model, the efficacy of the externally bonded CFRP plate for reinforcement was studied. In summary:

(1) By externally bonding the CFRP plate (with entire length and width), the stiffness and bearing capacity of the joint can be significantly increased (approximately 2.5 times and 1.7 times that of the original joint, respectively). Thus, the CFRP plate has a good potential for the application in segment joint reinforcement.

(2) The bonding length and width have a great influence on the strengthening effect. The insufficient bonding length and bonding width will lead to a significant weakening of the strengthening effect. According to the analysis results, it is recommended to adhere the CFRP plate to the entire area at the bottom as much as possible.

Through this study, it has been demonstrated that CFRP plates have the capability to reinforce shield segment joints from a mechanical perspective. Additionally, due to the excellent corrosion resistance of CFRP compared to steel, it has great potential for engineering applications.

It should be noticed that this paper only studied the strengthening effect of CFRP plates on joints under positive bending moments. The reinforcing effect of CFRP under negative bending moments still needs to be further investigated in subsequent research.

Data Availability

The data are available from the corresponding author upon reasonable request.

Conflicts of Interest

The authors declare that they have no conflicts of interest.

Acknowledgments

This study was funded by the Natural Science Foundation of Fujian Province (2023J01938) and the Scientific Research Startup Foundation of Fujian University of Technology (GY-Z21026 and GY-Z21067).

References

[1] S.-M. Liao, F.-L. Peng, and S.-L. Shen, "Analysis of shearing effect on tunnel induced by load transfer along longitudinal direction," *Tunnelling and Underground Space Technology*, vol. 23, no. 4, pp. 421–430, 2008.

[2] S. Megally, F. Seible, and R. K. Dowell, "Seismic performance of precast segmental bridges: segment-to-segment joints subjected to high flexural moments and low shears," *PCI Journal*, vol. 48, pp. 80–97, 2003.

[3] Z. Yan, H. Zhu, J. W. Ju, and W. Ding, "Full-scale fire tests of RC metro shield TBM tunnel linings," *Construction and Building Materials*, vol. 36, pp. 484–494, 2012.

[4] W. Ding, Y. Peng, Z. Yan, B. Shen, H. Zhu, and X. Wei, "Full-scale testing and modeling of the mechanical behavior of shield TBM tunnel joints," *Structural Engineering and Mechanics: An International Journal*, vol. 45, no. 3, pp. 337–354, 2013.

[5] X. Li, Z. Yan, Z. Wang, and H. Zhu, "A progressive model to simulate the full mechanical behavior of concrete segmental lining longitudinal joints," *Engineering Structures*, vol. 93, pp. 97–113, 2015.

[6] M. H. Al-Sherrawi, A. A. Allawi, B. H. Al-Bayati, M. Al Gharawi, and A. El-Zohairy, "Behavior of precast prestressed concrete segmental beams," *Civil Engineering Journal*, vol. 4, no. 3, pp. 488–496, 2018.

[7] A. Allawi, M. Al-Sherrawi, B. AL-Bayati, M. Al Gharawi, and A. El-Zohairy, "Experimental investigation of segmental post-tensioned girders: proceedings of the 2018 annual conference on experimental and applied mechanics," in *Challenges in Mechanics of Time-Dependent Materials*, pp. 87–94, Springer, Cham, 2019.

[8] Z. Li, K. Soga, F. Wang, P. Wright, and K. Tsuno, "Behaviour of cast-iron tunnel segmental joint from the 3D FE analyses and development of a new bolt-spring model," *Tunnelling and Underground Space Technology*, vol. 41, pp. 176–192, 2014.

[9] A. Fahimifar and M. R. Zareifard, "A new elasto-plastic solution for analysis of underwater tunnels considering strain-dependent permeability," *Structure and Infrastructure Engineering*, vol. 10, no. 11, pp. 1432–1450, 2013.

[10] N.-A. Do, D. Dias, P. Oreste, and I. Djeran-Maigre, "Three-dimensional numerical simulation for mechanized tunnelling in soft ground: the influence of the joint pattern," *Acta Geotechnica*, vol. 9, no. 4, pp. 673–694, 2014.

[11] H. Zhao, X. Liu, Y. Bao, Y. Yuan, and Y. Bai, "Simplified nonlinear simulation of shield tunnel lining reinforced by epoxy bonded steel plates," *Tunnelling and Underground Space Technology*, vol. 51, pp. 362–371, 2016.

[12] Q. J. Chen, J. C. Wang, W. M. Huang, Z. X. Yang, and R. Q. Xu, "Analytical solution for a jointed shield tunnel lining reinforced by secondary linings," *International Journal of Mechanical Sciences*, vol. 185, Article ID 105813, 2020.

[13] G. Yan, Y. Shen, B. Gao, Q. Zheng, K. Fan, and H. Huang, "Damage evolution of tunnel lining with steel reinforced rubber joints under normal faulting: an experimental and numerical investigation," *Tunnelling and Underground Space Technology*, vol. 97, Article ID 103223, 2020.

[14] G. Tiberti, G. A. Plizzari, J. C. Walraven, and C. Blom, "Concrete tunnel segments with combined traditional and fiber reinforcement," in *Tailor Made Concrete Structures*, pp. 199–204, Taylor & Francis Group, London, 2008.

[15] A. Caratelli, A. Meda, Z. Rinaldi, and P. Romualdi, "Structural behaviour of precast tunnel segments in fiber reinforced concrete," *Tunnelling and Underground Space Technology*, vol. 26, no. 2, pp. 284–291, 2011.

[16] Z. Wu-zhou, Z. Yi-xin, Z. Dong-ming, W. U. Hui-ming, and H. Hong-wei, "Numerical study on shearing performance of steel plate strengthened circumferential joints of segmental tunnel linings," *Chinese Journal of Geotechnical Engineering*, vol. 41, pp. 235–239, 2019.

[17] X. Liu, Q. Sun, W. Song, and Y. Bao, "Numerical modeling and parametric study of hybrid fiber-rebar reinforced concrete tunnel linings," *Engineering Structures*, vol. 251, Article ID 113565, 2022.

[18] Z. Li, X. Liu, H. Lai, Z. Yang, and B. Wang, "Detailed damage mechanism of deformed shield tunnel linings reinforced by steel plates," *Engineering Failure Analysis*, vol. 143, Article ID 106850, 2023.

[19] X. Liu, Y. Liu, Z. Jiang, J. Wang, and H. A. Mang, "Numerical investigation of the mechanical behavior of segmental tunnel linings reinforced by a steel plate—concrete composite structure," *Engineering Structures*, vol. 276, Article ID 115350, 2023.

[20] X. Liu, Z. Jiang, and H. A. Mang, "Experimental investigation of the bearing capacity of deformed segmental tunnel linings strengthened by a special composite structure," *Structure and Infrastructure Engineering*, vol. 19, no. 2, pp. 147–163, 2023.

[21] C. M. Lopez, I. Carol, and A. Aguado, "Meso-structural study of concrete fracture using interface elements. I: numerical model and tensile behavior," *Materials and Structures*, vol. 41, no. 3, pp. 583–599, 2008.

[22] C. M. Lopez, I. Carol, and A. Aguado, "Meso-structural study of concrete fracture using interface elements. II: compression, biaxial and Brazilian test," *Materials and Structures*, vol. 41, no. 3, pp. 601–620, 2008.

[23] X. F. Wang, Z. J. Yang, J. R. Yates, A. P. Jivkov, and C. Zhang, "Monte Carlo simulations of mesoscale fracture modelling of concrete with random aggregates and pores," *Construction and Building Materials*, vol. 75, pp. 35–45, 2015.

[24] Y. Huang and S. Hu, "A cohesive model for concrete mesostructure considering friction effect between cracks," *Computers and Concrete, An International Journal*, vol. 24, pp. 51–61, 2019.

[25] U. De Maio, F. Fabbrocino, F. Greco, L. Leonetti, and P. Lonetti, "A study of concrete cover separation failure in FRP-plated RC beams via an inter-element fracture approach," *Composite Structures*, vol. 212, pp. 625–636, 2019.

[26] W. Zhang, Z. Tang, Y. Yang, and J. Wei, "Assessment of FRP—concrete interfacial debonding with coupled mixed-mode cohesive zone model," *Journal of Composites for Construction*, vol. 25, no. 2, Article ID 4021002, 2021.

[27] Y. Huang, W. Zhang, and X. Liu, "Assessment of diagonal macrocrack-induced debonding mechanisms in FRP-strengthened RC beams," *Journal of Composites for Construction*, vol. 26, no. 5, Article ID 4022056, 2022.

[28] U. De Maio, F. Greco, L. Leonetti, P. N. Blasi, and A. Pranno, "An investigation about debonding mechanisms in FRP-strengthened RC structural elements by using a cohesive/volumetric modeling technique," *Theoretical and Applied Fracture Mechanics*, vol. 117, Article ID 103199, 2022.
[29] E. D. B. Comite, *CEB-FIP model code 1990: Design code*, Thomas Telford Publishing, 1993.
[30] B. Wu, Y. Luo, and J. Zang, "Experimental study on mechanical performance of tunnel segment joints strengthened using concrete-filled steel tubes," *Journal of Building Structures*, vol. 40, pp. 105–112, 2020.
[31] Simulia, "Abaqus analysis user's guide, version 6.14," in *Dassault Systemes*, Providence, RI, 2014.
[32] W. Zhang, S. Kang, Y. Huang, and X. Liu, "Behavior of reinforced concrete beams without stirrups and strengthened with basalt fiber-reinforced polymer sheets," *Journal of Composites for Construction*, vol. 27, no. 2, Article ID 4023007, 2023.